

## High-energy x-ray diffraction study of pure amorphous silicon

Khalid Laaziri

*Groupe de Recherche en Physique et Technologie des Couches Minces, Département de Physique, Université de Montréal,  
Case Postale 6128, Succursale Centre-Ville, Montréal (QC), Canada H3C 3J7*

S. Kycia

*CHESS, Wilson Laboratory, Cornell University, Ithaca, New York 14853*

S. Roorda\* and M. Chicoine

*Groupe de Recherche en Physique et Technologie des Couches Minces, Département de Physique, Université de Montréal,  
Case Postale 6128, Succursale Centre-Ville, Montréal (QC), Canada H3C 3J7*

J. L. Robertson

*Neutron Scattering Group, Solid State Division, Oak Ridge National Laboratory, Oak Ridge, Tennessee 37831-6393*

J. Wang<sup>†</sup> and S. C. Moss

*Department of Physics, University of Houston, Houston, Texas 77204-5506*

(Received 30 December 1998; revised manuscript received 16 April 1999)

Medium and high-energy x-ray diffraction has been used to study the atomic structure of pure amorphous Si prepared by MeV Si implantation into crystalline silicon. Both as-implanted and annealed samples were studied. The inelastically scattered x rays were removed by fitting the energy spectrum for the scattered x rays. The atomic scattering factor of silicon, previously known reliably up to  $20 \text{ \AA}^{-1}$ , has been extended to  $55 \text{ \AA}^{-1}$ . The radial distribution function of amorphous Si, before and after annealing, has been determined through an unbiased Fourier transformation of the normalized scattering data. Gaussian fits to the first neighbor peak in these functions shows that scattering data out to at least  $40 \text{ \AA}^{-1}$  is required to reliably determine the radial distribution function. The first-shell coordination number increases from 3.79 to 3.88 upon thermal annealing at  $600 \text{ }^\circ\text{C}$ , whereas that of crystalline Si determined from similar measurements on a Si powder analyzed using the same technique is 4.0. Amorphous Si is therefore under coordinated relative to crystalline Si. Noise in the distribution function, caused by statistical variations in the scattering data at high-momentum transfer, has been reduced without affecting the experimental resolution through filtering of the interference function after subtracting the contribution of the first-neighbor peak. The difference induced by thermal annealing in the remainder of the radial distribution functions, thus revealed, is much smaller than previously believed.

[S0163-1829(99)00943-1]

### I. INTRODUCTION

The atomic scale structure of amorphous solids, which have no spatial periodicity, yields diffuse diffraction patterns. x-ray neutron, and electron diffraction experiments have been used to characterize the structure of such materials. From the Fourier transform of the diffraction pattern, a correlation function between pairs of atoms, the radial distribution function (RDF), can be deduced. The RDF is, to a certain extent, a very useful representation of the topology of an amorphous network, as it contains information such as the characteristic distances associated with different neighbor pairs, the mean bond angles, and the coordination number of the first-neighbor peak. However, it is a one-dimensional representation of the structure of amorphous solids because of their isotropic nature. In order to discern the three-dimensional atomic structure, one must construct models, such as continuous random network<sup>1-8</sup> (CRN) models, and compare their RDF's with those obtained experimentally. Structural models that are quite distinct may therefore yield RDF's that are only slightly different. Hence, accurate radial

distribution functions with high spatial resolution are needed to discriminate among models for the actual atomic structure. This resolution is also essential in revealing subtle differences among samples prepared and annealed in various ways.

Synchrotron radiation sources have made available high-intensity photon beams at wavelengths much shorter than those used for conventional x-ray scattering experiments. Thus much larger momentum transfers,  $Q = 4\pi \sin \theta / \lambda$ , are accessible, which in turn makes much higher real-space resolution of the RDF's possible. In the present study the  $Q$  range was extended to  $55 \text{ \AA}^{-1}$ , which corresponds to a real-space resolution of  $0.1 \text{ \AA}$ . However, the use of high-energy x rays introduces a number of experimental difficulties. At high  $Q$ , the Compton contribution to the total scattering is often considerably larger than the coherent contribution for amorphous materials composed of light atoms like Si. In order to extract the integrated elastic scattering, it is important that one is able to separate the Compton from the elastic scattering. Also, the atomic scattering factor,  $f_{\text{Si}}$ , for Si is not well determined for  $Q$  values beyond  $\sim 20 \text{ \AA}^{-1}$ . This

problem can be dealt with relatively easily for amorphous silicon by using an analytical procedure to extend  $f_{\text{Si}}$  to larger  $Q$ , assuming that the scattering data are sufficiently accurate at high  $Q$ . In addition to problems associated with measurements at high x-ray energy, there are other inherent difficulties that are present when constructing RDF's from the diffraction data. In particular, the Fourier transform of a finite collection of data suffers from termination effects. These can be reduced by damping functions, but at the price of reduced spatial resolution. Alternatively, a sampling method can be used. Finally, careful attention should be paid to the accuracy of the instrumental alignment, sample mounting, statistics, correction procedures (dead time, absorption, multiple scattering, and so on), and data analysis as each of these can introduce experimental artifacts in the final RDF.<sup>9</sup>

Another aspect of the accuracy of the RDF of amorphous Si involves the obvious need for amorphous material of high purity and good homogeneity for the scattering experiment. Early measurements of the RDF of *a*-Si (Refs. 10 and 11) concluded that evaporated *a*-Si contains voids. Other studies<sup>12-17</sup> used material containing significant amounts of impurities such as O, Ar, or H. Plasma- or chemical-vapor-deposited hydrogenated *a*-Si, though of very high quality electronically, contains by design a few at. % of hydrogen. Amorphous silicon made by sputtering typically contains a similar percentage of the sputtering agent, whereas *a*-Si made by vacuum evaporation tends to peel off the substrate even before the layer thickness reaches one micron. More importantly, almost all *a*-Si made by deposition techniques contains voids<sup>10,18</sup> that may reach several nm in size and represent a volume fraction of several at. %. This means that a considerable fraction of the atoms sit at an internal surface and are not fully coordinated. The origin of the void structure may be related to the fact that every atom in the deposited *a*-Si was a surface atom during some stage of the deposition process. One way to avoid the inclusion of voids is to prepare *a*-Si directly from the crystalline or liquid phase. For this study we used MeV self-ion implantation, which typically yields only a few microns of *a*-Si. By using several implantation energies for the silicon ions, the thickness of the amorphous layer can be extended to greater than 10  $\mu\text{m}$ . Recently, small angle x-ray scattering (SAXS) measurements on *a*-Si made by such multi-MeV ion implantation<sup>19</sup> demonstrated the void-free nature of this material. Interestingly, studies on *a*-Si prepared by ion implantation, which is free of voids have shown that the amorphous state is less dense<sup>20,21</sup> than the crystalline state with a density deficit of 1.8%, and this deficit remains the same for as-implanted and thermally annealed *a*-Si.

In this paper, we will describe a detailed study of the determination and analysis of the RDF of amorphous silicon in the as-implanted and annealed state, compared with that of a crystalline silicon powder under similar experimental conditions. The experimental details of the high-energy x-ray scattering measurements covering a  $Q$  range from 0.03 to 55  $\text{\AA}^{-1}$ , as well as the details of the data analysis will be discussed. In addition, we will present a method for removing the Compton scattering, describe how the atomic scattering factor  $f_{\text{Si}}$  can be extended to larger  $Q$ , and demonstrate a procedure for filtering noise from the RDF. Our results show that even for fundamental information such as the nearest-

TABLE I. Ion energies and doses used for amorphizing a 12- $\mu\text{m}$  surface layer of *c*-Si.

Ion Energy (MeV)	0.5;1.5;2.0;3.5	5;7;9	11.5;14;17;20	23;27
Fluence (Si ions/cm <sup>2</sup> )	$5 \times 10^{15}$	$6 \times 10^{15}$	$8 \times 10^{15}$	$9 \times 10^{15}$

neighbor coordination number, diffraction data out to at least 40  $\text{\AA}^{-1}$  in  $Q$  is required. The majority of results presented in the literature (for amorphous materials in general) do not extend beyond 25  $\text{\AA}^{-1}$ . We find that amorphous silicon is slightly under coordinated with respect to a fourfold coordinated continuous random network, which explains why amorphous silicon is less dense than its crystalline counterpart. The high-resolution RDF's also allow us to resolve a long-standing issue directly related to the atomic structure of amorphous silicon, namely the nature of the structural relaxation induced by thermal annealing (1 h at 600 °C).<sup>22</sup> This structural relaxation can be understood as the removal of about 2 at. % of point self-defects, which contradicts an earlier description of structural relaxation in terms of a reduction in the average bond-angle distortion—a view that implies that every atom contributes equally to the structural relaxation.

## II. EXPERIMENT

### A. Sample preparation

Edge-supported amorphous silicon membranes were prepared<sup>23</sup> by implanting  $\langle 100 \rangle$  *p*-type Cz silicon substrates (resistivity of 1–10  $\Omega$ ) with  $\text{Si}^+$  ions at different energies and doses (see Table I) at liquid nitrogen temperature. The implantations were carried out at the 6 MV Van de Graaff Tandem Accelerator located at the Université de Montréal. The samples were then chemically etched from the back side of the implanted surface, in order to remove all the crystalline substrate, using a solution of KOH (20%) at a temperature of 80 °C and under continuous magnetic stirring; the etch rate was about 1.2  $\mu\text{m}/\text{min}$ . The KOH temperature was held constant during the etching process. This procedure resulted in pure *a*-Si membranes of 10 and 11  $\mu\text{m}$  thickness as measured by interferometry and energy loss of energetic protons. One of the two samples was then annealed under vacuum at a temperature of 600 °C for 1 h in order to induce structural relaxation. The other sample remained “as-implanted.” Raman spectroscopy was performed on the etched interface to make sure that no crystalline material was left. Elastic recoil detection in conjunction with time of flight was used to check the concentration and the depth profile of trace elements at the etched interface, and it was found that, apart from a small surface contamination, the concentration of C, O, and H was less than 0.1 at. %.

After the chemical etch, a slight buckling was observed of both membranes. Because *a*-Si is less dense than *c*-Si, both the amorphous film and the underlying substrate are somewhat stressed after the ion implantation. From wafer-curvature measurements during the implantation, it has been shown that the stress is largest just before a continuous

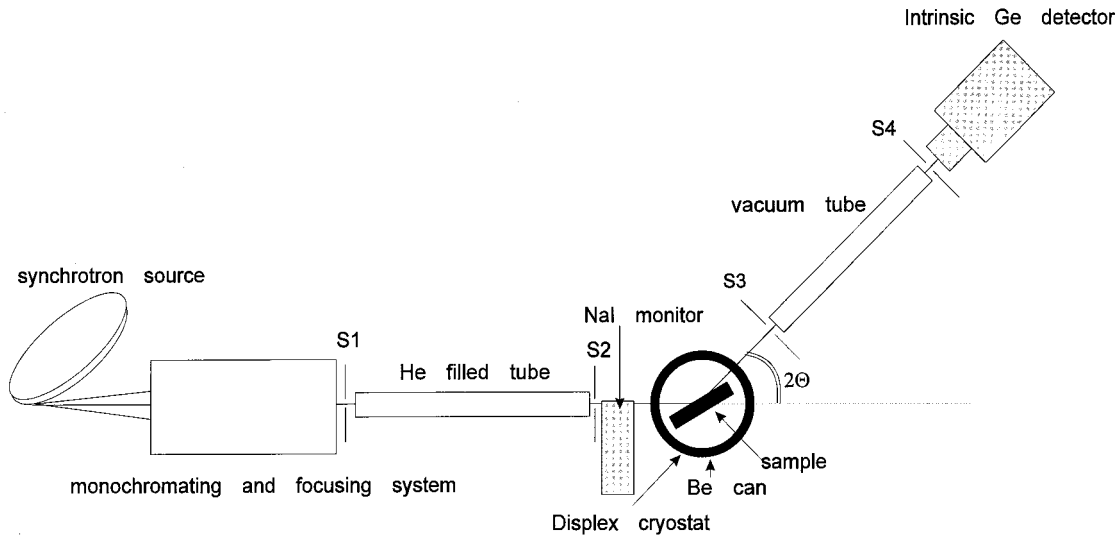


FIG. 1. Schematic diagram of the experimental configuration.

amorphous layer is formed, and that the stress relaxes through viscous flow of the *a*-Si (even at liquid nitrogen temperatures) during and immediately after the implantation.<sup>24</sup> However, not all the stress is relieved, and we observe that after removal of the crystalline backing, the membranes are indeed slightly larger than the circular hole they are spanning, which leads to the slight buckling of the membranes. Both membranes (as-implanted and annealed) were similarly buckled. The x-ray scattering was performed roughly in the middle of the membrane, far from the edges, where the stress should be almost completely relieved. Raman scattering on these same positions (reported in Ref. 23) showed a TO-like band (and shift induced by annealing) as would normally be observed in *a*-Si. We believe, therefore, that mechanical stress does not play a significant role in the different atomic structures observed here. In fact, since the majority of work on *a*-Si concerns thin films on a substrate, mechanical stresses should play a much smaller role here, than in almost all experimental results published to date.

High-purity silicon powder (reference 640b from the National Institute of Standards and Technology) with an average particle diameter less than 10  $\mu\text{m}$  was used as a crystalline reference sample. The silicon powder was pressed onto a 1.5-cm diameter polished disk (thickness of 2 mm). A solution of 1% of solvent based adhesive, diluted with acetone, was used to hold the fine silicon particles together. Since only a very small amount of the solution was used, less than 1 ml, the scattering from the adhesive can be safely ignored.

### B. X-ray diffraction

The experimental arrangement for the diffraction measurements is shown schematically in Fig. 1. It incorporates a focusing and monochromating system which consists of a Si(111) double-bounce monochromator with a sagittally bent second crystal for focussing the x-ray beam horizontally down to 1 mm. The slits ( $S_1$  and  $S_2$ ) just before the sample were used to define a 1 mm high and 3 mm wide incident beam. A NaI scintillator placed between  $S_2$  and the sample was used as a monitor. The samples were placed in a Displex cryostat (Model CSA-202A) mounted on Huber 6-circle diffractometer to cool the samples to 10 K in order to minimize thermal atomic vibrations, which damp the structure factor  $S(Q)$  and thus broaden the peaks in the RDF. A beryllium can under vacuum was used to cover the sample holder system, preventing condensation and air scattering.

The measurements on *a*-Si were carried out at the station A2-wiggler beamline of the Cornell High Energy Synchrotron Source (CHESS, Wilson Laboratory). In order to cover a large region in  $Q$  space from 0.5 to 55  $\text{\AA}^{-1}$ , four x-ray energies (13, 21.74, 43.57, and 60.1 keV) were used in reflection and, for the low- $Q$  scans, transmission geometry. With this choice of energy and geometry, it was always possible to resolve experimentally the incoherent Compton scattering from the coherent elastic scattering. The  $Q$  scans were taken at regular intervals  $\Delta Q = 0.025 \text{\AA}^{-1}$ . Table II summarizes the experimental configuration of this experiment. The

TABLE II. Experimental parameters for x-ray scattering of amorphous silicon.

Region	I	II	III	IV	V
$2\theta$ ( $^\circ$ )	59–130	45–130	54–130	44–129	4–57
$Q$ ( $\text{\AA}^{-1}$ )	30–55	17–40	10–20	4.9–11.9	0.5–6.25
$\Delta Q$ ( $\text{\AA}^{-1}$ )	0.025	0.025	0.025	0.025	0.025
$E$ (keV)	60.1	43.569	21.74	13	13
Geometry	Reflection	Reflection	Reflection	Reflection	Transmission
$\Phi$ ( $^\circ$ )	44 $^\circ$	44 $^\circ$	44 $^\circ$	40 $^\circ$	100 $^\circ$

$Q$  range measured at each energy was chosen to have overlapping regions between the scans. During each measurement the sample position was maintained at a fixed angle  $\phi$  (angle between the incident beam and the sample). The scattered x rays were detected using an intrinsic Ge solid-state detector with a 160 eV resolution. The signal from the detector was processed by a multichannel analyzer (MCA) and a complete energy scan was recorded for each value of  $Q$  thus allowing the Compton scattering to be removed.

The powder diffraction measurements on crystalline silicon were carried out at the CHESS C station using a 40.7-keV x-ray beam. The same experimental setup described above for the amorphous samples was used for this experiment, except that the measurements were all done in transmission. Two sets of multiple scans were performed: First, a  $Q$  range from 8 to 35  $\text{\AA}^{-1}$  was covered at regular  $Q$  steps of  $\Delta Q = 0.01 \text{\AA}^{-1}$ , then a second one for low- $Q$  scans from 1.5 to 10  $\text{\AA}^{-1}$  at  $\Delta Q = 0.005 \text{\AA}^{-1}$ . For the second series of scans, the beam was attenuated so that the Bragg peaks did not saturate the solid-state detector. The powder scans were performed using a  $\theta/2\theta$  geometry with an offset applied to the sample angle,  $\phi = \theta + \text{offset}$ , where  $\theta$  is half the scattering angle  $2\theta$ . The offset was varied for each scan by  $2^\circ$  to a total range of  $\pm 8^\circ$  in order both to minimize texture effects often observed for powder crystalline samples and to obtain a better powder average.

For both the amorphous and crystalline Si measurements, multiple scans were recorded. Each scan had sufficient counting statistics for a full analysis including the Fourier transform and peak fitting of the resulting radial distribution functions. This allowed us to determine the variance in the fitting results and use those to estimate the uncertainty in the final results.

### III. DATA ANALYSIS

The corrected intensity for both the amorphous and the crystalline powder samples is of the form

$$I_{\text{corr}} = \frac{I_{\text{exp}}}{M(\theta)A(\theta)V(\theta)} \left[ \beta + \frac{(1-\beta)}{P(\theta)} \right], \quad (1)$$

where  $I_{\text{exp}}$  is the experimentally measured elastic intensity corrected for background, dead time, and, for the crystalline Si, multiple scattering, and illuminated volume as well.  $\beta$  is the fraction of polarized x rays ( $\beta = 0.93$  for A2 station and  $\beta = 0.85$  for C station),  $M(\theta)$  the multiple scattering,  $A(\theta)$  the absorption,  $P(\theta)$  the polarization, and  $V(\theta)$  the volume correction. For amorphous silicon,  $V(\theta) = 1$  since there was no need for this correction. Each of these correction terms are discussed in the following sections.

#### Background and dead-time correction

In order to make accurate corrections for the instrumental background, some measurements were made with the sample removed, but with the full sample environment in place including the sample holder. In general, the dead-time correction factor for the counting system used can be expressed as:

$$C_T = \frac{C_0}{1 - C_0\tau}, \quad (2)$$

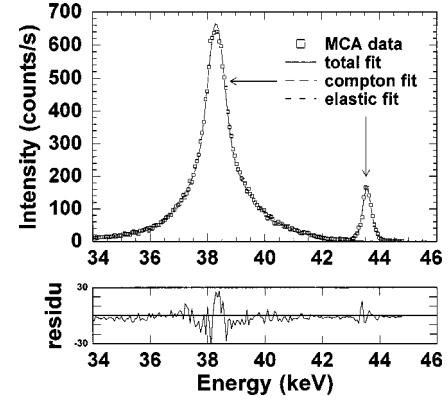


FIG. 2. Total x-ray scattering energy spectra at  $Q = 40 \text{\AA}^{-1}$  as measured (open squares) and fit (lines). Bottom panel shows residuals (incident x-ray energy is 43.6 keV).

where  $C_T$ ,  $C_0$  are the true and observed number of counts in the detecting system, respectively and  $\tau$  is the dead-time constant. Both the monitor and the solid-state detector were corrected for dead time. The respective dead-time constants  $\tau_m$  and  $\tau_d$  were determined by the multiple-foil method.<sup>25,26</sup> Typically,  $\tau_m \sim 6 \mu\text{s}$ , while the values for  $\tau_d$  values were ranging from 15 to 30  $\mu\text{s}$  for the range of x-ray energies used during the experiment.

#### Compton correction

The Compton inelastic scattering intensity  $I(Q)$  was subtracted from the experimental MCA energy spectra using a fitting procedure developed previously.<sup>27</sup> Basically, the MCA spectra were fit using a function of the form  $F(x) = E(x) + C_0(x)$  where  $E(x)$  is an asymmetric peak function corresponding to the elastic peak and  $C_0(x)$  is a theoretical Compton profile derived from the impulse approximation.<sup>28-30</sup> The shape parameters for the asymmetric peak function were only determined once for each x-ray energy, whereas the Compton profile was calculated for each scattering angle  $2\theta$ . The fits to the energy spectra were achieved with only two free parameters, namely, the amplitudes of the elastic and Compton contributions. The amplitude of the Compton scattering was included in the fit because, although the impulse approximation gives accurate shapes for the Compton scattering profile as a function of  $2\theta$ , it underestimates the intensity at large  $Q$ . Figures 2 and 3 show examples of the fits for low- and high- $Q$  scans. After fitting each energy spectrum,  $C_0(x)$  was subtracted from the spectrum and the spectrum was integrated to get the true experimental elastic scattering intensity. The purpose of the asymmetric peak function was solely to aid in the separation of the Compton and elastic contributions.

#### Multiple scattering

A multiple scattering correction was performed to obtain the experimental singly scattered elastic intensity.<sup>31,32</sup> The following correction was used:

$$I_{\text{exp single}} = \frac{i_{\text{mes}}}{(1 + R)}, \quad (3)$$

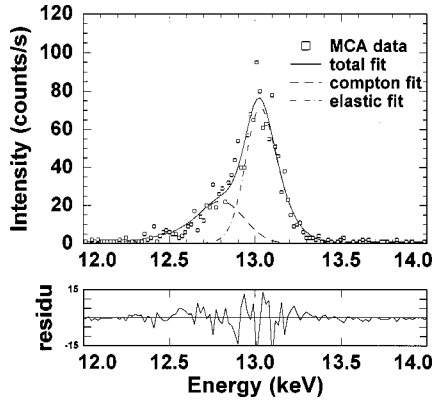


FIG. 3. Total x-ray scattering energy spectra at  $Q=7 \text{ \AA}^{-1}$  as measured (open squares) and fit (lines). Bottom panel shows residuals (incident x-ray energy is 13 keV).

where  $I_{\text{mes}}$  is the experimentally measured elastic intensity and  $R=I_{\text{mult}}/I_1$  is a calculated ratio between double and single scattering (courtesy of Simon Billinge, Michigan University). The multiple scattering correction is applied to the elastic intensity only, before the absorption and polarization corrections. For the thin-amorphous silicon membranes the multiple scattering is completely negligible, but for the much thicker crystalline powder Si sample it amounted to  $\sim 2\%$  of the elastic intensity.

### Absorption

X rays passing through a sample are partially absorbed by an amount depending on the total pathlength of the incident and scattered beam. Therefore a correction to the measured intensity must be applied. The absorption correction for both the reflection and transmission geometry has been deduced from the general expression,

$$A(\theta) = \frac{1}{V} \int_V e^{-\mu(L_1+L_2)} dV, \quad (4)$$

where  $V$  is the illuminated volume of the sample and  $L_1$  and  $L_2$  are the incident and scattered path lengths. For the reflection geometry,

$$A(\theta) = \frac{s}{V\mu} \frac{\sin(2\theta - \phi)}{\sin(2\theta - \phi) + \sin\phi} [1 - e^{-\mu t(1/\sin\phi - 1/\sin(2\theta - \phi))}] \quad (5)$$

and for the transmission geometry

$$A(\theta) = \frac{s}{V\mu} \frac{\sin(\phi - 2\theta)}{\sin(\phi - 2\theta) - \sin\phi} [e^{-\mu t/\sin(\phi - 2\theta)} - e^{-\mu t/\sin\phi}], \quad (6)$$

where  $s$  is the cross section of the incident beam,  $V$  the sample volume,  $\mu$  the absorption coefficient,  $t$  the thickness of the sample, and  $\phi$  the incident angle. The factor  $\mu t$  has been measured for the amorphous and powder crystalline silicon samples at each of the energies used during the experiment and are listed in Table III. Typically, the absorption corrections were in the order of 3% for the  $a$ -Si samples, and 12% for powder  $c$ -Si.

TABLE III. Experimentally determined absorption coefficient for silicon.

Energy (keV)	60	43.569	21.74	13
$\mu$ (cm <sup>2</sup> /g)	0.0164	0.490	3.7718	13.643

### Volume correction

A volume correction is needed to correct for the fraction of irradiated volume seen by the detector as defined by the slits in front of the detector, and it varies with scattering angle,  $2\theta$ ,

$$V(\theta) = \frac{1}{2} \left[ \frac{l^2}{\sin\theta \cos\theta} - \tan\theta \left( \frac{l}{\sin\theta} - t \right)^2 \right], \quad \theta < \theta_c \quad (7)$$

$$= \frac{1}{2} \frac{l^2}{\sin\theta \cos\theta}, \quad \theta > \theta_c, \quad (8)$$

where  $l=1$  mm is the vertical height of the incoming beam,  $t=1.7$  mm the thickness of the  $c$ -Si powder sample and  $\theta_c=36^\circ$  is the critical angle where the irradiated volume becomes smaller than that defined by the detector slits. This correction was not needed for the  $a$ -Si samples, because the area defined by the detector slits was larger than the irradiated volume in all the range of scattering angles  $2\theta$ .

### Polarization factor

The x rays were highly polarized (around 90% for beam-line station A2, and 85% for station C). Once the majority of the corrections were applied to the intensity data, we used the fraction of polarized x rays as a free parameter (within limits) to adjust the overlap between the  $Q$  scans corresponding to the different energies. A value of 93% turned out to give the best agreement between the overlap regions for  $a$ -Si (station A2), and 85% for  $c$ -Si powder (station C). The remaining intensities, 7 and 15 % for the  $a$ -Si and the powder  $c$ -Si sample respectively, were then corrected for polarization using the factor,

$$P(\theta) = \frac{(1 + \cos^2 2\theta)}{2}. \quad (9)$$

Typically, the polarization corrections were of the order of 3% for  $a$ -Si, and 8% for the  $c$ -Si powder.

### Verification of correction procedure

Figure 4 shows the different overlap regions obtained by matching the corrected intensities for  $a$ -Si. It can be seen that the overlap between the different regions is good to within 1%, indicating that the various corrections were applied correctly. In order to illustrate the effects of errors that might be introduced by a problem with one of the corrections, we arbitrarily changed the fraction of polarized x rays  $\beta$ , by  $\pm 5\%$ . The error introduced into the polarization correction by reducing  $\beta$  by 5% and its dramatic effect on the overlapping regions are shown in Fig. 5. However, when  $\beta$  is increased by 5% the polarization correction still seems to give satisfactory results. In summary, this test indicates that the scattering data are sensitive to small errors in the correction

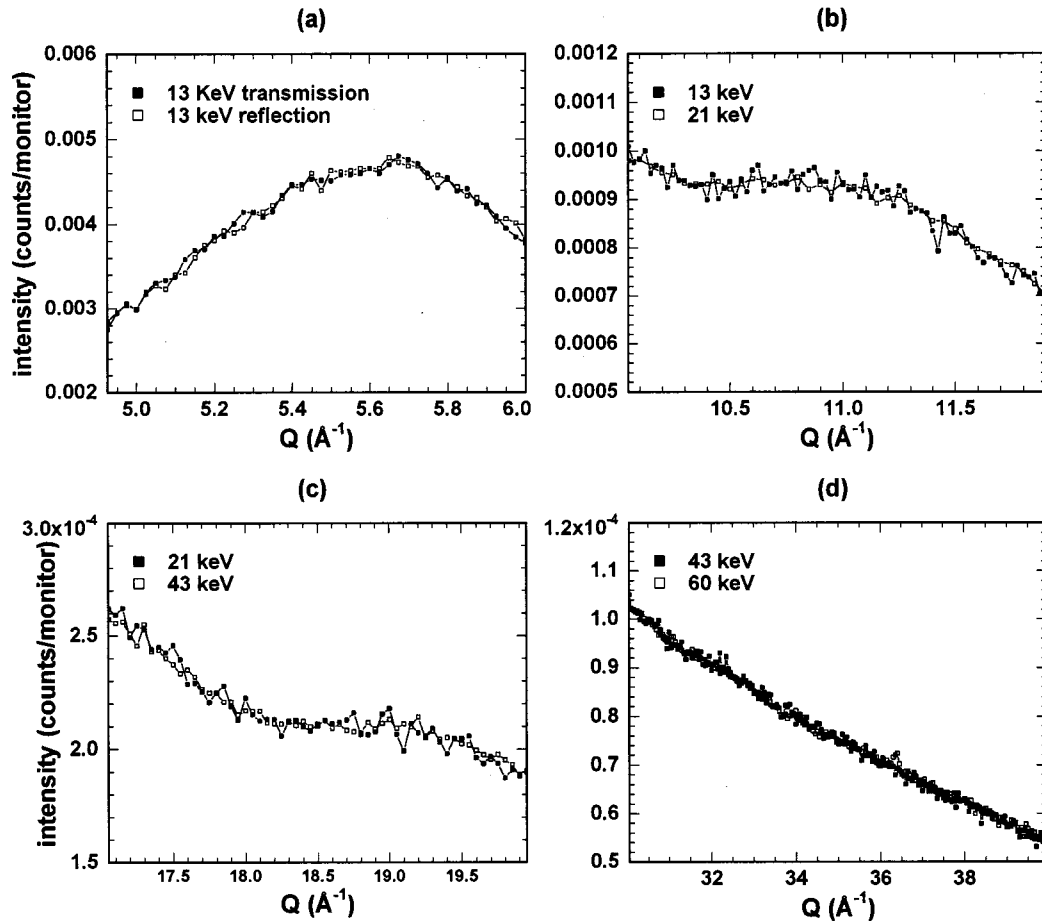


FIG. 4. Intensity of x ray scattered from amorphous silicon in the “overlap” regions, showing the agreement between different geometries or energies: (a) at 13 keV between transmission and reflection, (b) between 13 and 21 keV reflection, (c) between 21 and 43 keV in reflection, and (d) between 43 and 60 keV in reflection.

procedures. Fortunately, the overlapping regions will usually indicate when there is a problem.

#### Atomic scattering factor

In order to normalize the corrected intensity  $I_{\text{corr}}$  to electron units (e.u.), we needed to deduce an atomic form factor

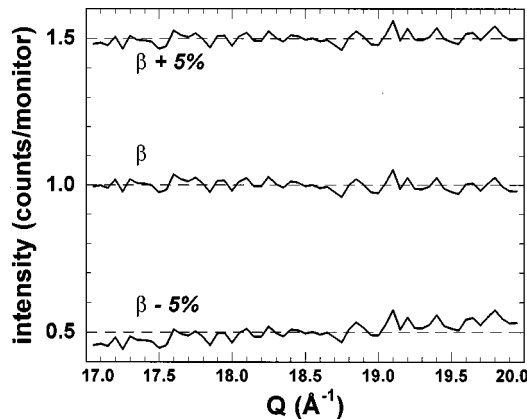


FIG. 5. The amorphous silicon intensity ratio in the overlap region, between 21 and 43 keV, for different choices of the polarization correction constant: for  $\beta=93\%$  used during the correction, for a 5% larger  $\beta$  value offset by +0.5, and for a 5% smaller value of  $\beta$  offset by -0.5.

for Si,  $f_{\text{Si}}$ , from the data.  $f_{\text{Si}}$  is reliably known up to  $Q \sim 20 \text{ \AA}^{-1}$  and this was used as a starting point. The elastic scattering intensity from the amorphous samples oscillates around  $f^2$  until the oscillations die out at large  $Q$ .  $f_{\text{Si}}^2$  was expanded to larger  $Q$ , as follows:

- (1) We used the previously determined value<sup>33</sup> of  $f_{\text{Si}}$  from 0 to  $20 \text{ \AA}^{-1}$  to roughly normalize the data to e.u. The normalization factor was calculated following the method of Krogh-Moe<sup>34</sup> and Norman.<sup>35</sup>
- (2) A new intensity is constructed as illustrated in Fig. 6. From 0 to  $20 \text{ \AA}^{-1}$  the intensity was replaced by  $f_{\text{Si}}^2$ , from 20 to  $30 \text{ \AA}^{-1}$  the original scattering data was retained, and from 30 to  $Q_{\text{temp}} = 35 \text{ \AA}^{-1}$  (a temporary maximum) the scattered intensity was replaced with heavily smoothed data. This fabricated intensity was then fit using a series of exponential functions; the resulting fit corresponds then to a new, interim  $f_{\text{Si}}^2$ . Steps 1 and 2 are repeated iteratively by varying the value of  $Q_{\text{temp}}$  from  $35 \text{ \AA}^{-1}$  until the whole range is covered ( $0-55 \text{ \AA}^{-1}$ ). Using the literature value for  $f$  from 0 to  $20 \text{ \AA}^{-1}$  forces the expanded  $f$  to coincide with the literature value in that range.
- (3) The resulting function was then fit by a monotonically decreasing analytical function

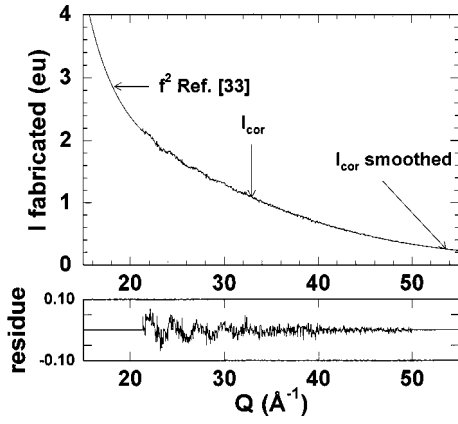


FIG. 6. The intensity constructed (see text) to fit the extended region of  $f_{\text{Si}}^2$ . The residue is shown in the bottom panel.

$$f(Q) = c + \sum_{i=1}^5 a_i \exp(-b_i Q^2) \quad (10)$$

in order to avoid spurious effects due to statistical variations during the process. The fitted parameters are listed in Table IV. With this single set of parameters, the scattered data from both *a*-Si and the powder *c*-Si samples could be satisfactory analyzed.

#### Fourier transform and termination ripples

The structure factor is defined as

$$S(Q) = \left( \frac{I(Q)}{f^2} \right), \quad (11)$$

where  $I(Q)$  is the fully corrected and normalized coherent scattering intensity. The interference function is defined as,

$$F(Q) = Q \times [S(Q) - 1]. \quad (12)$$

The Fourier transform of the structure factor,  $G(r)$ , called the reduced radial distribution function, is given by

$$G(r) = \frac{2}{\pi} \int_0^{\infty} Q [S(Q) - 1] \sin Qr dQ, \quad (13)$$

from which we derive the radial distribution function,  $J(r)$ ,

TABLE IV. Coefficients for the analytical expression of the scattering factor of silicon.

Parameters	Deduced $f(0-55 \text{ \AA}^{-1})$
$c$	0.207976
$a_1$	3.67842
$a_2$	3.84222
$a_3$	1.56637
$a_4$	0.528977
$a_5$	4.17884
$b_1$	3.31157
$b_2$	41.2418
$b_3$	0.091511
$b_4$	131.486
$b_5$	1.49295

$$J(r) = 4\pi r^2 \rho(r) = 4\pi r^2 \rho_0 + rG(r) \quad (14)$$

and

$$T(r) = 4\pi r \rho_0 + G(r), \quad (15)$$

where  $\rho(r)$  is the number density function of the actual atomic structure and  $\rho_0$  is the average atomic density of the sample.

The ideal Fourier transform of  $Q[S(Q) - 1]$  in principle requires data from  $Q=0$  to  $Q=\infty$ . However, the range of  $Q$  values that is obtained from experiment is limited to a finite value,  $Q_{\text{max}}$ . This will introduce ‘‘termination ripples’’ of wavelength  $2\pi/Q_{\text{max}}$  into the RDF and causes a broadening of  $J(r)$  due to the cut-off function,  $H(Q)$ ,

$$H(Q) = 1, \quad 0 < Q < Q_{\text{max}} \\ = 0, \quad Q > Q_{\text{max}}. \quad (16)$$

Consequently, the actual  $G(r)$  obtained by Fourier transforming the experimental data is given by

$$G(r) = \frac{2}{\pi} \int_0^{\infty} H(Q) Q [S(Q) - 1] \sin Qr dQ. \quad (17)$$

In other words, the measured  $G(r)$  is a convolution of the true correlation function and the peak function,

$$P(Q) = \frac{1}{\pi} \int_0^{\infty} H(Q) \cos Qr dQ. \quad (18)$$

The peak function  $P(Q)$ , with a peak height of  $Q_{\text{max}}/\pi$  and a FWHM (full width at half maximum) of  $3.8/Q_{\text{max}}$ , yields a broadening of  $\Delta r = 0.07 \text{ \AA}$  when  $Q_{\text{max}} = 55 \text{ \AA}^{-1}$ . This broadening occurs in each peak of  $J(r)$ .

The problem of termination ripples can be lessened, to a certain extent, in several ways. Many authors have used damping functions when dealing with termination ripples where they multiply the interference function  $F(Q)$  with a modification function  $M(Q)$  in order to obtain a gradual cut-off. This procedure replaces the sharp discontinuity at  $Q_{\text{max}}$  by a more smoothly varying function. Two common damping functions are used in reducing termination ripples: One is the Lorch function<sup>36</sup>

$$M(Q) = \frac{Q_{\text{max}}}{\pi Q} \sin\left(\frac{\pi Q}{Q_{\text{max}}}\right), \quad \text{for } 0 < Q < Q_{\text{max}}, \quad \text{and} \\ = 0 \quad \text{for } Q > Q_{\text{max}}, \quad (19)$$

in which case the corresponding peak function  $P_L(Q)$  has a FWHM of  $5.437/Q_{\text{max}}$ , broadening the real space resolution to  $\Delta r = 0.098 \text{ \AA}$  when  $Q_{\text{max}} = 55 \text{ \AA}^{-1}$ . The other damping function often used is the exponential function<sup>37</sup>

$$M(Q) = \exp(-BQ^2), \quad \text{for } 0 < Q < Q_{\text{max}}, \quad \text{and} \\ = 0 \quad \text{for } Q > Q_{\text{max}}. \quad (20)$$

There is no consensus as to the most appropriate value of  $B$  in the literature; in most cases,  $B$  is chosen so that

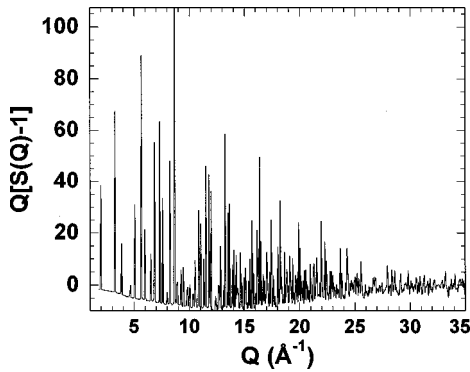


FIG. 7. The interference function of powder *c*-Si determined by x-ray diffraction.

$M(Q_{\max})=0.1$  or less. These methods do indeed reduce the termination ripples, but at a price of broadening the peaks in  $J(r)$ .

An alternative to the use of damping functions is the so-called “sampling” method.<sup>38</sup> Here, we only use interference functions that terminate with a value of 0 at the upper integration limit. In other words, the RDF is calculated only for  $r$  values that satisfy the following condition that

$$r = n \frac{\pi}{Q_{\max}} \quad \text{or} \quad r = (2n+1) \frac{2\pi}{Q_{\max}}, \quad \text{where } n = 1, 2, 3 \dots$$

In this case, every point in the RDF is thus the result of an unbiased Fourier transform of the  $S(Q)$  data and no damping function is used. The density of points in real space is limited because of the restrictions imposed by the sampling procedure. However, in reality this reflects the true spatial resolution. In practice the use of the sampling method should only be considered if the scattering data cover a sufficiently large region of  $Q$  space to get a sufficiently dense set of points in  $J(r)$ . Since our data extends to  $55 \text{ \AA}^{-1}$ , use of the sampling method is appropriate.

## IV. RESULTS

### A. Powder crystalline silicon

In order to test the accuracy of the procedure for determining the RDF of *a*-Si the RDF of *c*-Si was determined through diffraction measurements of a crystalline powder sample (described in the sample preparation section) for  $Q$  between 1 and  $35 \text{ \AA}^{-1}$ .

Figure 7 shows the structure factor of *c*-Si, which includes both Bragg peaks and diffuse scattering contributions. The Bragg peak intensities are likely to suffer from preferred orientation effects, since it is difficult to obtain powder samples with completely random orientation. The Fourier transform  $G(r)$  of the crystalline powder data calculated using the sampling method is shown in Fig. 8. For  $r < 2 \text{ \AA}$ ,  $G(r)$  oscillates around  $-4\pi\rho_0 r$ , where  $\rho_0 = 0.04997 \text{ \AA}^{-3}$  is the known average atomic density of *c*-Si. The large oscillation near  $r=0$  (thin solid line) is attributed to slowly varying errors in  $F(Q)$  and is likely due to an error in the normalization constant. In order to correct for this problem we have used a procedure due to Kaplow.<sup>39</sup> The low- $r$  region ( $< r_{\min} = 1.5 \text{ \AA}$ ) of  $G(r)$  was back Fourier transformed, and

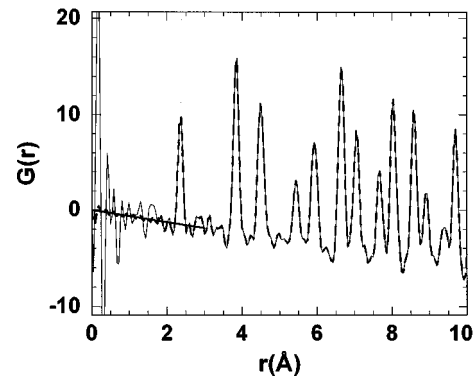


FIG. 8. The reduced radial distribution function  $G(r)$ , of powder *c*-Si before (—), and after (---) the Kaplow correction.

subtracted from  $F(Q)$ ; the resulting  $G(r)$  is shown as a dashed line in Fig. 8. The solid and dashed lines overlap everywhere except at  $r < 2 \text{ \AA}$ , which indicates that the correction only affects the low- $r$  region without changing the RDF peaks containing the structural information.

A direct comparison between our data from the sampled Fourier transform and the known structure of *c*-Si is shown in Fig. 9. Here, the solid line is the  $J(r)$  for the diamond structure with a lattice constant of  $5.431 \text{ \AA}$ , where each peak is broadened to have a Gaussian distribution. For the first peak  $\sigma_1 \sim 0.06 \text{ \AA}$  and for the other peaks  $\sigma \sim 0.08 \text{ \AA}$  (nearest neighbors do not vibrate against each other with the same amplitude as uncorrelated distant neighbors). The broadening is a combined effect of thermal disorder and the experimental resolution of the Fourier transform. The dots represent a single-sampled point of the Fourier transform. All the points fall quite close to the solid line (and continue to do so much beyond the maximum range of  $10 \text{ \AA}$  shown here). In particular, the positions and heights of the first two peaks are in excellent agreement with the solid line as will be discussed further in the section “coordination vs  $Q_{\max}$ ” where the effect of  $Q_{\max}$  on the results is examined. This coincidence leads us to conclude that high energy x-ray diffraction, as analyzed by the method described in this paper, yields an accurate and reliable determination of the RDF.

### B. Amorphous silicon

The corrected and normalized elastic intensities  $I(Q)$ , of both the as-implanted (dotted line) and annealed (solid line)

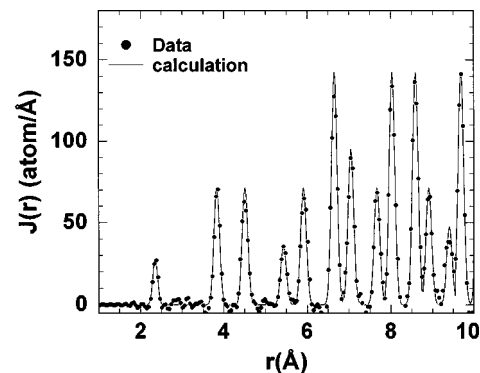


FIG. 9. The radial distribution function  $J(r)$ , of powder crystalline silicon as measured (dots). The solid line represents a theoretical calculation of the crystalline  $J(r)$  broadened by a Gaussian distribution.

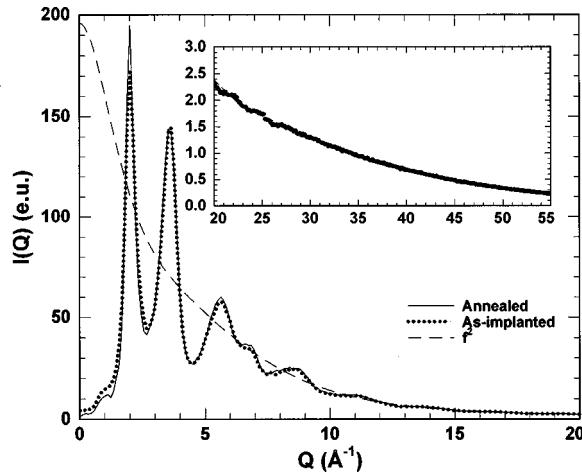


FIG. 10. The normalized intensity in electron units  $I(Q)$ , of the as-implanted (dotted line), and annealed (solid) amorphous silicon membranes, overlaid on  $f_{\text{Si}}^2$  (dashed). The inset plot represents the extension of the plot to large  $Q$ .

amorphous silicon are shown in Fig. 10. Clearly,  $I(Q)$  oscillates about  $f_{\text{Si}}^2$  until the oscillations damp out at large  $Q$ . The two intensities are almost identical, except at low  $Q$ , indicating differences in the atomic structure beyond the first-neighbor distance. These normalized intensities were used to determine the interference functions,  $F(Q)$ , for both materials. We have added results from earlier small angle x-ray scattering (SAXS) measurements<sup>19</sup> to the high-energy synchrotron data in order to achieve a total  $Q$  range from 0.03 to 55  $\text{\AA}^{-1}$ . In Fig. 11, we display the structure factor,  $S(Q)$ , as determined for both the annealed and as-implanted *a*-Si. The inset shows the corresponding interference function  $F(Q)$ . Oscillations in structure factors are clearly visible up to  $\sim 40 \text{\AA}^{-1}$ . Beyond this value the statistical noise drowns out the oscillations. Again a small difference can be seen between the two structure factors at low  $Q$  as noted above.

#### Fourier transform and noise reduction

The Fourier transform  $G(r)$ , calculated for both the as-implanted and annealed *a*-Si samples using the sampling

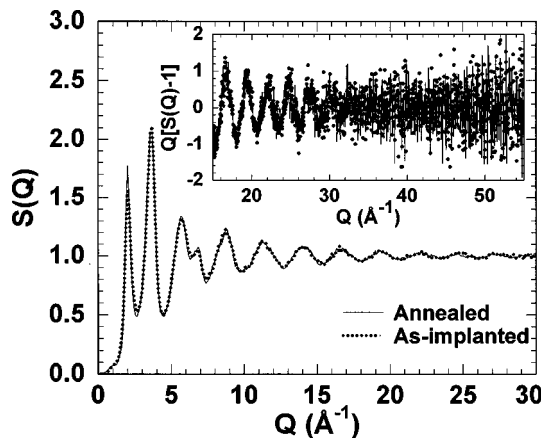


FIG. 11. The structure factor  $S(Q)$ , of the as-implanted (dots) and annealed (line) amorphous silicon membranes. The inset plot represents the corresponding interference functions  $F(Q)$ , of the two samples in the high- $Q$  region.

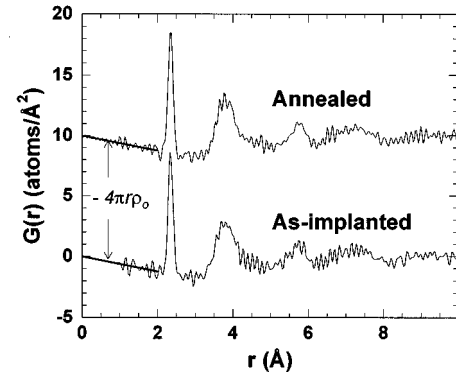


FIG. 12. The reduced radial distribution function  $G(r)$ , of amorphous Si “as-implanted” and annealed at 600 °C (offset by 10 atoms/ $\text{\AA}^2$ ). The straight lines from which  $-4\pi r\rho_0$  is determined are also shown ( $\rho_0=0.049$  atoms/ $\text{\AA}^3$ ).

method is shown in Fig. 12. For  $r < 2 \text{\AA}$ , both curves oscillate linearly around  $-4\pi\rho_0 r$ , where  $\rho_0$  is the average atomic density. By least squares fitting, it was deduced that  $\rho_0=(0.0489\pm 0.004) \text{\AA}^{-3}$ , a value that was identical for the two materials to within 0.1% and which is in excellent agreement with previous density measurements of *a*-Si (Refs. 20 and 21) where  $\rho_0=0.0492 \text{\AA}^{-3}$ . In  $G(r)$ , we can see the presence of noise, which we attribute to the statistical noise in  $F(Q)$  for large  $Q$ , as well as a significant ripple throughout, due to the way the data was binned. Realizing that it is primarily the first-neighbor peak that determines  $S(Q)$  for  $Q$  beyond 20  $\text{\AA}^{-1}$ , we have adopted the following procedure to reduce this noise and ripple: The first-neighbor peak in the RDF was isolated and its contribution to the interference function evaluated through a reverse Fourier transform. This contribution was subtracted from the interference function, and the remaining signal which, beyond  $Q=20 \text{\AA}^{-1}$ , is essentially statistical noise only, is damped through multiplication by a factor  $\exp[-\alpha(Q/Q_{\text{max}})^2]$ , where  $\alpha=8$ , and  $Q_{\text{max}}=55 \text{\AA}^{-1}$ . The unfiltered first-neighbor contribution is then added back to the filtered data, as illustrated in Fig. 13 which shows both the filtered (dotted line) and the unfiltered (solid line)  $F(Q)$ . The resulting interference function is then Fourier transformed to yield the new filtered  $J(r)$ . Figure 14 shows  $J(r)$  for both materials, filtered (solid line) and unmodified (dots). This filtering procedure was efficient in sup-

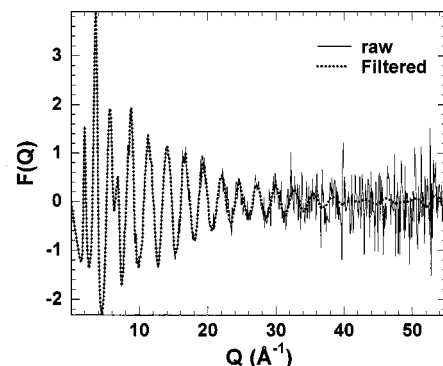


FIG. 13. The interference functions of annealed *a*-Si,  $F(Q)$ , before (solid line) and after (dotted lines) filtering the noise at large  $Q$ .

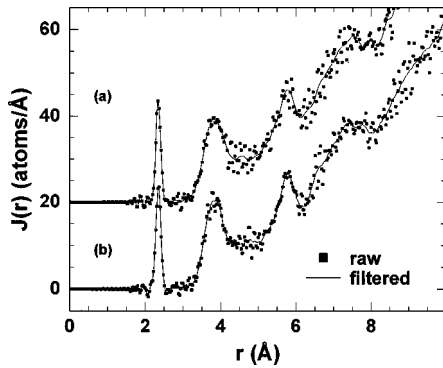


FIG. 14. The RDF of the as-implanted (a) and annealed  $a$ -Si (b) sample calculated before (squares) and after (solid line) filtering the noise from  $F(Q)$  at large  $Q$  as described in the text.

pressing the noise from  $J(r)$ , without affecting the resolution and without altering the termination ripples inherent in the Fourier transform.

In Fig. 15, we show the resulting RDF's of both the annealed ( $\lambda$ ) and the as-implanted ( $\text{---}$ )  $a$ -Si samples from 1 to 5 Å. The first-neighbor peaks of both samples are nearly indistinguishable. Note that the height of the second-neighbor peak increases upon thermal annealing. Surprisingly, the widths of the second-neighbor peaks remain almost identical. In the region between the second and third peak, at around 4.7 Å, a small enhancement in the annealed RDF over the as-implanted RDF can be seen. This observation suggests the existence of a peak seen earlier by Moss and Graczyk.<sup>10</sup> We do not believe that this peak is spurious, since it appears at the same position in all the RDF's calculated using different values of  $Q_{\max}$ . The existence of such a peak can be indicative of dihedral bond-angle ordering<sup>40,41</sup> (the dihedral angle is defined as the angle of rotation about a common bond of two tetrahedral units). In fact, it seems that there is a preferential orientation of the neighboring tetrahedral unit in the annealed  $a$ -Si, which is reflected by a narrower distribution, compared to the as-implanted  $a$ -Si where the dihedral angle distribution should be quite large. (This peak may also be construed as a weak tendency of  $a$ -Si to reflect the third-neighbor peak of  $c$ -Si.<sup>10</sup>)

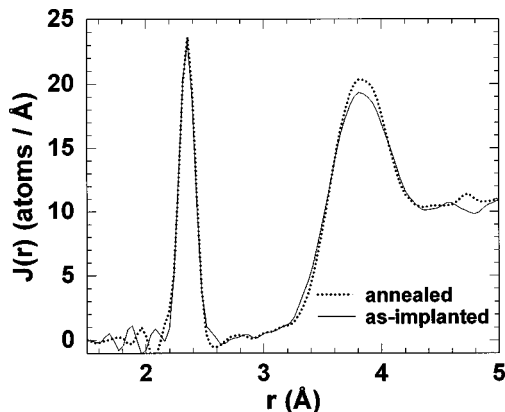


FIG. 15. The first two peaks of the radial distribution function  $J(r)$ , of annealed (solid line) and as-implanted (dotted line) amorphous Si.

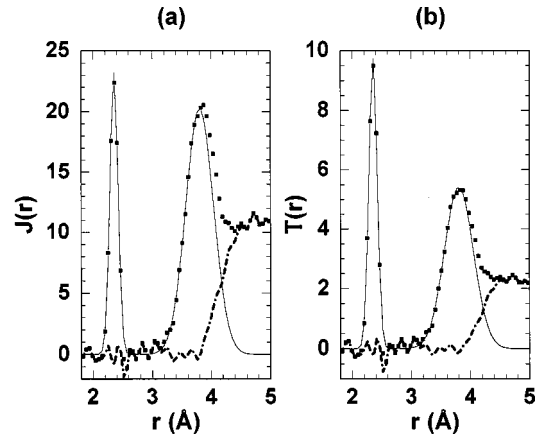


FIG. 16. Gaussian fits (solid lines) of the first, and lower half of the second peaks of the function  $J(r)$  [squares, (a)], and  $T(r)$  [squares, (b)]. The dotted-dashed curve is the residual (Gaussian fits subtracted from data).

#### Peak fitting

A full interpretation of the RDF requires extensive modeling of the atomic structure, but basic structural data of the short-range atomic order can be extracted by simply fitting the individual peaks of the RDF—at least those that can be resolved. Since the first peak of the RDF of both crystalline and amorphous silicon is well separated from all the other peaks, the average coordination number  $C_1$  of first-neighbor Si-Si atom distribution can be evaluated with reasonable accuracy by fitting both  $J(r)$  and  $T(r)$  to a Gaussian profile. We also used a peak fitting function, corresponding to the contribution of the first peak in  $Q$  space, in order to fit  $F(Q)$ . The fitting function for  $T(r)$  was of the form

$$t_i(r) = \frac{C_i}{r} \frac{e^{-(r-r_i)^2/2\sigma_i^2}}{\sqrt{2\pi\sigma_i^2}}, \quad (21)$$

for  $J(r)$  of the form,

$$j_i(R) = r t_i(r) \quad (22)$$

and for  $F(Q)$  ( $Q$  space) of the form,

$$f_i(Q) = C_i \frac{\sin r_i Q}{r_i} e^{-1/2 Q^2 \sigma_i^2} \quad (23)$$

where  $C_i$  is the coordination number in the  $i$ th shell,  $r_i$  the position of the  $i$ th distribution, and  $\sigma_i^2$  is the mean-square amplitude of thermal vibration plus mean-square static disorder. Fits to  $F(Q)$  were done using data starting at  $15.2 \text{ \AA}^{-1}$  in order to allow only contributions from next-neighbor distances. A typical real space fit of  $J(r)$  and  $T(r)$  is illustrated in Fig. 16.

The results of all the curve fits are listed in Table V. For both the as-implanted and the annealed  $a$ -Si samples the first-neighbor peaks were centered at  $r_1 \sim 2.35 \text{ \AA}$  and their total widths were  $\sigma_1 \sim 0.065 \text{ \AA}$ . A small but significant difference occurred in the coordination numbers, which were  $C_1 \sim 3.79$  for the as-implanted sample, and  $C_1 \sim 3.88$  for the annealed sample. Table V also lists uncertainties; these are determined from the variance of independent fits to five separate RDF's of each sample. The position, coordination

TABLE V. Peak fitting parameters for annealed, and as-implanted amorphous silicon ( $Q_{\max}=55 \text{ \AA}^{-1}$ ), and crystalline powder silicon ( $Q_{\max}=35 \text{ \AA}^{-1}$ ).

	As-implanted <i>a</i> -Si			Annealed <i>a</i> -Si			Crystalline powder Si	
	$t(r)$	$j(r)$	$f(Q)$	$t(r)$	$j(r)$	$f(Q)$	$t(r)$	$j(r)$
$C_1$	$3.786 \pm 0.01$	$3.79 \pm 0.01$	$3.787 \pm 0.12$	$3.882 \pm 0.01$	$3.881 \pm 0.004$	$3.886 \pm 0.12$	$4.032 \pm 0.04$	$4.021 \pm 0.05$
$r_1$	$2.349 \pm 0.001$	$2.351 \pm 0.001$	$2.349 \pm 0.04$	$2.351 \pm 0.001$	$2.352 \pm 0.001$	$2.351 \pm 0.004$	$2.354 \pm 0.003$	$2.356 \pm 0.004$
$\sigma_1$	$0.064 \pm 0.001$	$0.064 \pm 0.001$	$0.064 \pm 0.003$	$0.065 \pm 0.001$	$0.0065 \pm 0.001$	$0.065 \pm 0.003$	$0.057 \pm 0.003$	$0.0569 \pm 0.004$
$C_2$	$9.57 \pm 0.20$	$12.15 \pm 0.11$		$9.71 \pm 0.11$	$12.43 \pm 0.38$		$12.16 \pm 0.23$	$12.15 \pm 0.22$
$r_2$	$3.795 \pm 0.01$	$3.808 \pm 0.01$		$3.80 \pm 0.01$	$3.81 \pm 0.01$		$3.84 \pm 0.002$	$3.841 \pm 0.002$
$\sigma_2$	$0.259 \pm 0.006$	$0.257 \pm 0.006$		$0.242 \pm 0.008$	$0.238 \pm 0.006$		$0.066 \pm 0.002$	$0.066 \pm 0.002$

number, and the peak widths as determined from the fits of  $J(r)$  and  $T(r)$  were found to be equal to within 0.1%.

For the second-neighbor peak of the *a*-Si samples, the parameters are difficult to obtain since it contains contribution from more distant neighbor peaks. A crude estimation can be made by first assuming that the second-neighbor distribution is symmetric about  $r_2$ , and then considering only the lower half of the peak, which, to a certain extent, contains only the contribution from the second-neighbor correlations. Within the estimated errors, mainly introduced by choosing the upper  $r$  cutoff value between 3.75 and 3.9 Å, our best estimate of the *a*-Si second peak position was  $r_2 \sim 3.8$  Å. The coordination numbers were significantly different with  $C_2 \sim 12.15$  for the as-implanted *a*-Si and  $C_2 \sim 12.43$  for the annealed *a*-Si. The peak widths of the second-neighbor peaks were  $\sigma_2 \sim 0.258$  Å for the as-implanted *a*-Si and  $\sigma_2 \sim 0.240$  Å for the annealed *a*-Si.

## V. DISCUSSIONS

There are three main aspects of the results shown in the preceding sections that we wish to discuss further. First, the extent of our data and the simplicity of the material studied allow us to evaluate the reliability and precision of the different approaches to the Fourier analysis. Second, we can begin to examine what we can learn about the atomic structure of *a*-Si. We will examine the structure of annealed *a*-Si, which is believed to be the material closest to an ideal, four-fold coordinated continuous random network. Third, we will examine the changes in the structure of *a*-Si induced by thermal annealing.

### Reliability of radial distribution functions: coordination vs $Q_{\max}$

As a test of the accuracy of the coordination number it is important to consider it as a function of  $Q_{\max}$  because it is sensitive to artifacts introduced by the Fourier transform. In an earlier publication,<sup>42</sup> we showed how the first neighbor peak in the radial distribution function evolves as  $Q_{\max}$  is increased from 20 to 50  $\text{\AA}^{-1}$ . In Fig. 17, the variation of the coordination number of the first peak  $C_1$ , is shown as a function of  $Q_{\max}$ . The coordination number of each sample initially decreases with  $Q_{\max}$ , and then approaches a constant value around  $Q_{\max} \sim 40 \text{ \AA}^{-1}$ . Although the data on the *c*-Si powder only extend to  $Q_{\max} = 35 \text{ \AA}^{-1}$ , it is clear that the coordination number approaches a value of 4.0. For the

smaller values of  $Q_{\max}$ , the fitting procedure described above overestimates the coordination number because of the contribution from termination ripples. For large  $Q$ , the peak shape becomes independent of  $Q_{\max}$  with a mean value  $C_1$  of  $3.79 \pm 0.01$  for the as-implanted sample, and  $3.88 \pm 0.01$  for the annealed sample. Beyond  $Q_{\max} > 40 \text{ \AA}^{-1}$ , we believe that the intrinsic value for the position, coordination number, and width has been reached. This would indicate that even for a simple, single-atom system such as *a*-Si, reliable RDF's require scattering intensity data that extends to at least  $40 \text{ \AA}^{-1}$ .

Figure 18 illustrates the reliability (or lack thereof) of Lorch [Eq. (19), open squares] and exponential [Eq. (20), filled squares] damping functions. The figure shows the values obtained for  $C_1$  by performing Gaussian fits to the first neighbor peak in RDF's calculated using one of the damping functions, again as a function of the upper integration limit  $Q_{\max}$ . Fitting a Gaussian to a damped transform is effectively equivalent to fitting directly a peak function, as defined by Warren,<sup>43</sup> to an undamped RDF containing termination ripples. The figure also shows the variation in  $C_1$  as a function of  $Q_{\max}$  for sampled Fourier transformation (star symbols) for ‘‘as implanted’’ *a*-Si [Fig. 18(a)] and annealed *a*-Si [Fig. 18(b)]. All methods converge to the same value at large  $Q_{\max}$ , reinforcing our confidence in the experimental results. For small values of  $Q_{\max}$ ,  $< 30 \text{ \AA}^{-1}$ , the estimates of  $C_1$  based on damped functions seem to give values that approach the final  $C_1$  more closely than that based on a sampled Fourier transform. However, our results do call into

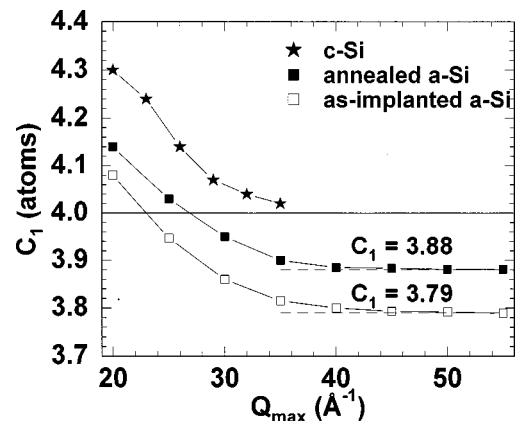


FIG. 17. Coordination number of the first-neighbor peak for as-implanted (open squares) and annealed (solid squares) *a*-Si, and that for crystalline Si powder (stars) as a function of  $Q_{\max}$ .

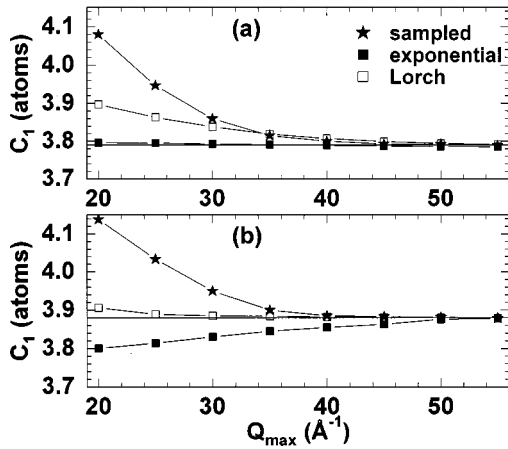


FIG. 18. Coordination number of the first-neighbor peak for as-implanted (a) and annealed (b) *a*-Si, as deduced from  $J(r)$  determined via sampling (stars), exponential damping [Eq. (20), solid squares], and Lorch damping [Eq. (19), open squares] as a function of  $Q_{\max}$ .

question the *reliability* of damping functions. In one sample [Fig. 18(a)], exponential damping gives a very good estimate but the Lorch-type damping is in error, while in the other sample [Fig. 18(b)] the Lorch-type damping estimates the final value correctly but exponential damping is off by a few percent. When scattering data beyond, say,  $30 \text{ \AA}^{-1}$  are not present, one would not know which method gives the best estimate. Estimates based on sampled transforms are farther off, but at least overestimate  $C_1$  by similar amounts in both samples.

#### Atomic structure of annealed amorphous Si material

The Gaussian fits to the nearest neighbor peak revealed an average bond length of  $(2.350 \pm 0.001) \text{ \AA}$ , compared to our measurement in *c*-Si of  $(2.355 \pm 0.004) \text{ \AA}$ . The *a*-Si bond length is, therefore, identical to that in *c*-Si to within  $0.005 \text{ \AA}$ . There is, of course, some static disorder. The width of the first-neighbor peak is partially due to this static disorder with additional contributions from thermal disorder and experimental resolution. The latter two contributions can be estimated by considering the corresponding value for *c*-Si where the width of the first peak should be dominated by the thermal motion and real space resolution. We found a peak width of  $0.057 \text{ \AA}$  for the *c*-Si powder. Assuming that the three contributions are independent, the corrected bond length variation in annealed *a*-Si is estimated to be  $0.031 \text{ \AA}$ . This small value illustrates the stiffness of the covalent Si-Si bond.

If the small difference in bond length,  $0.005 \text{ \AA}$ , were the only difference between *a*-Si and *c*-Si, then *a*-Si would be 0.6% denser than *c*-Si, but this is not what is observed. Both our present data (Fig. 12) and macroscopic density measurements<sup>20,21</sup> on void-free *a*-Si have shown that it is roughly 2% *less* dense than *c*-Si. This can now be understood as a consequence of undercoordination. The number of nearest neighbors  $C_1$ , obtained from Gaussian fits to the radial distribution function as described above, was found to be  $3.88 \pm 0.01$ , significantly less than 4. There are two different ways of accommodating such an undercoordination in an

otherwise fully connected fourfold-coordinated network. (1) If the undercoordination is solely due to *isolated* dangling bonds, then this number would imply a dangling bond density of 12%. (2) If the undercoordination is uniquely caused by network vacancies, then this number corresponds to 1 vacancy per 67 network sites [with ‘‘vacancy,’’ we mean an unoccupied network site; the four dangling bonds pointing into such a vacancy are expected to rearrange in various ways. Such network vacancies are surprisingly similar to the lattice vacancy in *c*-Si (Ref. 44)]. To put these two extreme views in context, we first realize that an *isolated* dangling-bond density of 12% is clearly much higher than what is experimentally observed. It is known from optical absorption,<sup>45</sup> electrical,<sup>46</sup> SAXS,<sup>47</sup> and combined Raman and positron lifetime measurements,<sup>48</sup> that only a few at. % H is required to saturate all dangling bonds. The required vacancy density of 1.5% is, however, much more reasonable as it corresponds closely to the density deficit of *a*-Si with respect to *c*-Si. Furthermore, a large number of experiments have shown that *a*-Si contains vacancy type defects, and that dangling bonds are rarely isolated but mostly associated with structural defects (see also the section below on structural relaxation). We therefore conclude that the undercoordination is mostly due to the presence of vacancy-type defects that result in the density deficit of *a*-Si with respect to *c*-Si.

The interpretation of the second-neighbor peak in the RDF is less certain because it suffers from an unknown contribution of the third-neighbor peak (Fig. 16). In the context of a random network containing vacancies, the coordination number of the second-neighbor peak  $C_2$  would be approximated by  $C_2 = C_1 \times [C_1 - 1]$ , yielding a value of  $C_2 = 11.18$ , whereas Gaussian fits yield a value of  $12.4 \pm 0.4$  atoms. The discrepancy could be due to the aforementioned contribution from the third peak, an asymmetry in the second peak, or to a deviation from the network structure. The width of the second peak  $\sigma_2 \sim 0.240 \text{ \AA}$  contains static disorder (arising from bond length  $a$  and bond-angle distortions), thermal vibration and experimental resolution. The thermal contribution can be subtracted from  $\sigma_2$ , again using the powder *c*-Si results, yielding to  $\sigma_{2,sl} = 0.23 \text{ \AA}$ , which would imply an average bond-angle distortion of  $\Delta\theta_b = (9.63 \pm 0.08)^\circ$ . This value for  $\Delta\theta_b$  is not unlike values reported in previous studies,<sup>10,14–17,29</sup> but nevertheless should be treated with some caution. The position of the second-neighbor peak was found to be at  $r_2 \sim 3.8 \text{ \AA}$ , which corresponds to an *average* bond angle of  $\theta_b = (107.83 \pm 0.97)^\circ$ . In the radial distribution function of *c*-Si, where the second and third peaks are well separated,  $r_2 \sim 3.84 \text{ \AA}$ , corresponding to  $\theta_b = 109^\circ 3$ . Again, the discrepancy could be due to a contribution from the third peak, an asymmetry in the second peak, or to a deviation from the ideal network structure. We once again stress that the analysis of the second-neighbor peak and beyond can be more reliably studied through computer modeling rather than through curve fitting.

#### Structural relaxation and defect annihilation

The purpose for studying two *a*-Si samples, one ‘‘as-implanted’’ and the other annealed at  $600^\circ \text{C}$  is to provide a comparison of their respective atomic structures and draw conclusions regarding the nature of the structural relaxation

induced by annealing. At the outset, it should be pointed out that structural relaxation is not densification, as the atomic density of ion-implanted *a*-Si is known to remain unchanged upon annealing to within 0.1%.<sup>20,21,24</sup> This is confirmed by our measurements, as both samples exhibit the same average density (see Fig. 14). (Densification can be observed in *a*-Si prepared by deposition techniques, if the growth conditions were such that a nano-porous structure was produced.<sup>10</sup>)

Comparing the nearest-neighbor peak in the RDF's from both *a*-Si samples, it is seen that the position and width remain unchanged (to within a *pm*), but that the area of the peak increases by 2%, from 3.79 to 3.88 atoms. A host of other techniques has shown that structural relaxation is accompanied by a reduction in the defect density of 2%, namely isothermal and scanning calorimetry,<sup>49</sup> positron spectroscopy,<sup>50</sup> Pd solubility and diffusivity measurements,<sup>51</sup> and hydrogen trapping.<sup>45</sup> This strongly implies that the increase in coordination number is a direct consequence of the reduction in defect density and reinforces our earlier conclusion that the final undercoordination indicates a remaining vacancy density of about 1.5%. However, it raises the question why structural relaxation is not accompanied by densification. It also raises the confusing question how the difference in coordination between *a*-Si and *c*-Si can be related to a density difference (see the discussion above) while at the same time, a similar difference between relaxed and as-implanted *a*-Si does not lead to a density difference. One possible explanation could be the presence of interstitial type defects, because it is known in *c*-Si that the volume change induced by equal numbers of vacancies and interstitials is essentially zero.

Interstitial-type defects would introduce atomic distances well removed from the main peaks in the RDF but would be difficult to observe because they represent a small fraction of the total number of atom pairs and the distances involved would not tend to peak sharply about any particular value. We have made an attempt to detect such interstitial-type defects in our RDF's by subtracting the Gaussian peak profiles from the fits to the first two peaks. Integrating the remaining RDF between the central positions of those peaks would give the added contributions from noise, termination ripples, and interstitial-type defects. Over a large enough region (from 2.35 to 3.84 Å, for example), the noise and termination ripple contribution should cancel, and only the contribution from the interstitial-type defects would remain. This procedure gave integrated values of about 0.12 and 0.07 atoms for "as-implanted" and annealed *a*-Si, respectively. (In *c*-Si, with much stronger termination ripples, the same procedure yields 0.03 atoms.) If these numbers do indeed represent interstitial-type defects, then the increase in coordination number induced by thermal annealing is balanced by a decrease in interstitial defects, thus conserving, as observed, average atomic density.

The Gaussian fit to the second-neighbor peak is less reliable than that to the first, but we estimate that the reliability problem is less serious for comparison purposes between the two *a*-Si samples than for absolute results. We thus compare the parameters of the second-neighbor peak from the two samples and observe that the peak position remains essentially unchanged after annealing, but both the area and the width change. The peak area increases upon thermal anneal-

ing, from 12.15 to 12.4 atoms. In the context of defect removal from an otherwise fully connected network, one would expect that  $C_2$  again can be approximated by  $C_2 = C_1 \times [C_1 - 1]$ . Thus we expect  $C_2$  to increase from 10.45 to 11.18 atoms, based on the first-neighbor coordination number in both samples. The observed increase in  $C_2$  is not as large as estimated, and this could be due to a contribution from interstitial-type defects or to the general unreliability in the Gaussian fits to the second peak, or both.

The other major difference between the second neighbor peak in our two samples is its width. It is seen that the peak width decreases significantly, implying a reduction in the average bond angle distortion induced by thermal annealing from  $(10.45 \pm 0.09)^\circ$  to  $(9.63 \pm 0.08)^\circ$ . We attribute the excess in distorted bonds to strained regions surrounding the defects<sup>52,53</sup> in as-implanted *a*-Si. Annihilation of the defects removes the strained regions, thus reducing the average bond-angle distortion.

Earlier experimental work on structural relaxation of *a*-Si either detected the average bond-angle distortion (Raman spectroscopy or low-resolution diffraction), or probed changes in the defect population (positron spectroscopy, carrier lifetime, impurity trapping, and diffusion). The high-resolution radial distribution functions presented here allow us to study both aspects, the defect removal (nearest-neighbor coordination number increase) and the associated reduction in average bond-angle distortion (width of second peak) in one measurement.

#### IV. CONCLUSIONS

In conclusion, we have presented a detailed account of our x-ray diffraction study of the atomic structure of pure amorphous Si. Multi-MeV ion implantation and a wet-chemical etch have been used to prepare edge-supported membranes of pure amorphous Si that are free of impurities, crystalline inclusions, and voids. X-ray diffraction has been performed at 13 to 60 keV photon energies up to a scattering vector of  $55 \text{ \AA}^{-1}$ . By recording and curve fitting the scattered energy spectrum at each scattering angle, the Compton incoherent scattering could be separated from the elastic signal carrying the structural information. Using the existing atomic factor  $f_{\text{Si}}$  of solid Si and our new data, which oscillates slowly around  $f_{\text{Si}}^2$ , we have extended  $f_{\text{Si}}$  from 20 to  $55 \text{ \AA}^{-1}$ . The extended range over which data were gathered allowed the use of the sampling method to obtain an unbiased Fourier transformation for the determination of the radial distribution function. Gaussian fits to these functions showed that the nearest neighbor distance in amorphous Si is identical to that in crystalline Si to within 0.005 Å and that the r.m.s. static disorder in bondlength amounts to  $\sim 0.03 \text{ \AA}$ . Both the bondlength and its static distortion remain essentially unchanged upon thermal annealing at 600 °C, but the nearest neighbor coordination number increases by 2% from 3.79 to 3.88, which still is one vacancy per 67 atoms short of perfect fourfold coordination. This explains why amorphous Si is less dense than crystalline Si. The increase in average number of nearest neighbors, and other subtle changes in the radial distribution functions induced by thermal annealing,

are consistent with an explanation of structural relaxation in amorphous Si in terms of the removal of 2 at. % of point defects.

### ACKNOWLEDGMENTS

This work is supported by the Natural Science and Engineering Research Council of Canada (NSERC) and the Fonds pour la formation de Chercheurs et l'Aide à la Recherche (FCAR). The Cornell High Energy Synchrotron Source

(CHESS) is supported by the National Science Foundation, under Award No. DMR-9311772. Work at the University of Houston was supported by the U.S. DOE/BES on Contract No. DE-FG05\_87ER 45325 and at Oak Ridge National Laboratory on Contract No. DE-AC05\_96OR 22464. It is a pleasure to thank D. L. Williamson for the SAXS measurements, Simon J. L. Billinge for the multiple-scattering corrections, Laurent Lewis for the theoretical *c*-Si RDF calculations and enlightening discussions, and Pierre Bérichon and Real Gosselin for expert technical assistance during ion implantation.

\*Electronic address: Sjoerd.Roorda@umontreal.ca

†Present address: Net Explorer, 4200 Montrose Blvd., Suite 45, Houston, TX 77005.

<sup>1</sup>D. E. Polk, *J. Non-Cryst. Solids* **5**, 365 (1971).

<sup>2</sup>D. E. Polk and D. S. Boudreaux, *Phys. Rev. Lett.* **31**, 92 (1973).

<sup>3</sup>F. Wooten, K. Winer, and D. Weaire, *Phys. Rev. Lett.* **54**, 1392 (1985).

<sup>4</sup>F. Wooten, and D. Weaire, in *Solid State Physics: Advances in Research Applications*, edited by D. Turnbull and H. Ehrenreich (Academic, New York, 1987), Vol. 40, p. 2.

<sup>5</sup>R. Car and M. Parrinello, *Phys. Rev. Lett.* **60**, 204 (1988).

<sup>6</sup>T. Uda, *Solid State Commun.* **64**, 837 (1988).

<sup>7</sup>R. Biswas, G. S. Crest, and C. M. Soukoulis, *Phys. Rev. B* **36**, 7437 (1987).

<sup>8</sup>G. A. N. Connell and R. J. Temkin, *Phys. Rev. B* **9**, 5323 (1974).

<sup>9</sup>B. J. Thijsse, *J. Appl. Crystallogr.* **10**, 61 (1984).

<sup>10</sup>S. C. Moss and J. F. Graczyk, *Phys. Rev. Lett.* **23**, 1167 (1969).

<sup>11</sup>S. C. Moss and J. F. Graczyk, in *Proceedings of the Tenth International Conference on Physics of Semiconductors, Cambridge, MA*, edited by S. P. Keller, J. C. Hesnel, and F. Stern (U.S. Atomic Energy Commission, Washington, D.C., 1970), p. 658.

<sup>12</sup>S. Kugler, G. Molnár, G. Pető, E. Zsoldos, L. Rosta, A. Menelle, and R. Bellissent, *Phys. Rev. B* **40**, 8030 (1989).

<sup>13</sup>S. Kugler, L. Pusztai, L. Rosta, P. Chieux, and R. Bellissent, *Phys. Rev. B* **48**, 7685 (1993).

<sup>14</sup>J. Fortner and J. S. Lannin, *Phys. Rev. B* **39**, 5527 (1989).

<sup>15</sup>R. Mosseri, C. Sella, and J. Dixmier, *Phys. Status Solidi A* **52**, 475 (1979).

<sup>16</sup>A. Menelle, A. M. Flak., P. Lagarde, and R. Bellissent, *J. Phys. C* **8**, 379 (1986).

<sup>17</sup>A. Filipponi, F. Evangelisti, M. Befatto, S. Mobilio, and C. R. Natoli, *Phys. Rev. B* **40**, 9636 (1989).

<sup>18</sup>I. Ohdomari, M. Kakumu, H. Sugahara, M. Mori, T. Saito, T. Yonehara, and Y. Hajimoto, *J. Appl. Phys.* **52**, 6617 (1981).

<sup>19</sup>D. L. Williamson, S. Roorda, M. Chicoine, R. Tabti, P. A. Stolk, S. Acco, and F. W. Saris, *Appl. Phys. Lett.* **67**, 226 (1995).

<sup>20</sup>J. S. Custer, M. O. Thompson, D. C. Jacobson, J. M. Poate, S. Roorda, W. C. Sinke, and F. Spaepen, *Beam-Solid Interactions: Physical Phenomena*, edited by J. A. Knapp, P. Børgesen, and R. Zuhr, MRS Symposia Proceedings No. 157 (Materials Research Society, Pittsburgh, 1990), p. 689.

<sup>21</sup>K. Laaziri, S. Roorda, and J. M. Baribeau, *J. Non-Cryst. Solids* **191**, 193 (1995).

<sup>22</sup>S. Roorda, W. C. Sinke, J. M. Poate, D. C. Jacobson, S. Dierker, B. S. Dennis, D. J. Egelsham, F. Spaepen, and P. Fuoss, *Phys. Rev. B* **44**, 3702 (1991).

<sup>23</sup>S. Roorda, K. Laaziri, and S. Gujrahi, *Nucl. Instrum. Methods Phys. Res. B* **148**, 360 (1998).

<sup>24</sup>C. A. Volkert, *J. Appl. Phys.* **74**, 7107 (1993).

<sup>25</sup>J. W. Müller, *Nucl. Instrum. Methods* **112**, 47 (1973).

<sup>26</sup>D. R. Chipman, *Acta Crystallogr., Sect. A: Cryst. Phys., Diffr., Theor. Gen. Crystallogr.* **25**, 209 (1969).

<sup>27</sup>K. Laaziri, J. L. Robertson, S. Roorda, M. Chicoine, S. Kycia, J. Wang, and S. C. Moss, *J. Appl. Crystallogr.* **32**, 322 (1999).

<sup>28</sup>J. W. M. Dumond, *Phys. Rev.* **33**, 643 (1929).

<sup>29</sup>P. Eisenberger and P. M. Platzman, *Phys. Rev. A* **2**, 415 (1970).

<sup>30</sup>J. B. Mann and J. T. Waber, *At. Data Nucl. Data Tables* **5**, 201 (1973).

<sup>31</sup>G. Malet, C. Cabos, A. Escande, and P. Delord, *J. Appl. Crystallogr.* **6**, 139 (1973).

<sup>32</sup>R. Serimaa, T. Pitkänen, S. Vahvaselkä, and T. Paakari, *J. Appl. Crystallogr.* **23**, 11 (1990).

<sup>33</sup>D. Waasmaier and A. Kierfel, *Acta Crystallogr., Sect. A: Found. Crystallogr.* **51**, 416 (1995).

<sup>34</sup>J. Krogh-Moe, *Acta Crystallogr.* **9**, 915 (1956).

<sup>35</sup>N. Norman, *Acta Crystallogr.* **10**, 370 (1957).

<sup>36</sup>E. Lorch, *J. Phys. C* **2**, 229 (1969).

<sup>37</sup>L. W. Bragg and J. West, *Philos. Mag.* **10**, 823 (1930).

<sup>38</sup>R. Lovell, G. R. Mitchell, and H. Windle, *Acta Crystallogr., Sect. A: Cryst. Phys., Diffr., Theor. Gen. Crystallogr.* **35**, 598 (1979).

<sup>39</sup>R. Kaplow, S. L. Strong, and B. L. Averbach, *Phys. Rev.* **138**, A1336 (1965).

<sup>40</sup>R. J. Temkin, W. Paul, and G. A. N. Connell, *Adv. Phys.* **22**, 581 (1973).

<sup>41</sup>R. J. Temkin, *J. Non-Cryst. Solids* **28**, 23 (1978).

<sup>42</sup>K. Laaziri, S. Kycia, S. Roorda, M. Chicoine, J. L. Robertson, J. Wang, and S. C. Moss, *Phys. Rev. Lett.* **82**, 3460 (1999).

<sup>43</sup>B. E. Warren, *X-ray Diffraction* (Dover, New York, 1969), p. 1990.

<sup>44</sup>G. N. van den Hoven, Z. N. Liang, L. Niesen, and J. S. Custer, *Phys. Rev. Lett.* **68**, 3714 (1992).

<sup>45</sup>K. F. Heidemann, M. Grüner, and E. te Kaat, *Radiat. Eff.* **82**, 103 (1984).

<sup>46</sup>S. Coffa and J. M. Poate, *Appl. Phys. Lett.* **59**, 2296 (1991).

<sup>47</sup>S. Acco, D. L. Williamson, P. A. Stolk, F. W. Saris, M. J. van den Boogaard, W. C. Sinke, W. F. van der Weg, S. Roorda, and P. C. Zalm, *Phys. Rev. B* **53**, 4415 (1996).

<sup>48</sup>Y. Hiroyama, T. Motooka, R. Suzuki, Y. Hirano, and F. Sato, *Appl. Phys. Lett.* **68**, 3126 (1996).

<sup>49</sup>S. Roorda, S. Doorn, W. C. Sinke, P. M. L. O. Scholte, and E. van Loenen, *Phys. Rev. Lett.* **62**, 1880 (1989).

<sup>50</sup>S. Roorda, R. A. Hakvoort, A. van Veen, P. A. Stolk, and F. W. Saris, *J. Appl. Phys.* **72**, 5145 (1992).

<sup>51</sup>S. Coffa, J. M. Poate, D. C. Jacobson, and A. Polman, *Appl. Phys. Lett.* **58**, 2916 (1991).

<sup>52</sup>A. Antonelli, E. Kaxiras and D. J. Chadi, *Phys. Rev. Lett.* **81**, 2088 (1998).

<sup>53</sup>H. Seong and L. J. Lewis, *Phys. Rev. B* **53**, 9791 (1996).